# SPATIAL DISTRIBUTION OF LASER LIGHT ABSORPTION BY SMALL SPHERES UNDERGOING MIE SCATTERING

by

David Black

A senior thesis submitted to the faculty of

Brigham Young University

in partial fulfillment of the requirements for the degree of

Bachelor of Science

Department of Physics and Astronomy

Brigham Young University

April 2010

BRIGHAM YOUNG UNIVERSITY

DEPARTMENT APPROVAL

of a senior thesis submitted by

David Black

This thesis has been reviewed by the research advisor, research coordinator, and department chair and has been found to be satisfactory.

| | |
|---|---|
| Date | Justin Peatross, Advisor |
| Date | Eric Hintz, Research Coordinator |
| Date | Ross L. Spencer, Chair |

ABSTRACT

# SPATIAL DISTRIBUTION OF LASER LIGHT ABSORPTION BY SMALL SPHERES UNDERGOING MIE SCATTERING

David Black

Department of Physics and Astronomy

Bachelor of Science

Our group has made a variety of observations regarding how small opaque particles can be levitated in a focused CW laser beam. The phenomenon relies on a radiometric effect, where the particle is heated by the laser and interacts with surrounding air molecules. Intuitively, one would expect opaque particles to heat up more on the sunny side and thus be propelled out of the beam. Thus, the mechanism by which some particles become trapped in the beam remains a mystery. The distribution of energy absorption within tiny, absorbing spheres ($\sim$10 wavelengths across) is investigated to try to gain insight into the levitation of small particles. This is computed using standard Mie scattering analysis as outlined in the textbook *Principles of Light and Optics* by Born and Wolf. [1] In our analysis, we concentrate on the internal fields rather than the scattered fields that are usually the subject of such analyses. We investigate whether there can be "shady-side heating," where

more energy is absorbed on the side of the particle opposite the direction of the beam propagation, which could potentially explain the trapping mechanism. It is found that there is no such effect.

# ACKNOWLEDGMENTS

A special thanks should be given right away to Dr. Justin Peatross, my advisor and a great help through the ups and downs of undergraduate life. My friends since freshman year and colleagues in research endeavors—Eric Cunningham and Jacob Johansen—deserve special mention as well. Dr. Peatross had the idea for the project and got me pushed in the right direction, teaching me much about research along the way. Eric and Jake have been with me since freshman year. Not only did they help me with this research project, but we have collaborated on the many research projects Dr. Peatross has allowed us to take on. They have helped me survive life as a physics major and as a person. I am grateful to Dieter Bauer of the University of Rockstock for discussing Mie theory with me and sharing insights he found in his research [2] as well as some of his code. Of course, I would like to thank my parents and brothers and sisters for their continued support, and especially my parents for the scientific teaching and motivation (among many other things) they gave me as I grew up.

# Contents

# List of Figures

# Chapter 1

# Introduction

## 1.1 Radiometric Levitation of Small Particles

A number of researchers have reported on the interaction between light and small dust particles. Microscopic particles have been observed doing interesting motion in a continuous laser beam. [4] Sometimes small (∼1-10 µm) particles become caught indefinitely in the focus. A number of researchers have reported this phenomenon. [3, 5, 6, 7] The particles observed are made of various materials, such as graphite, tungsten, and black liquor (a biproduct in the process of making paper). Many different shapes of particles have been trapped. The trapped particles are observed to light up brightly in the beam as they scatter light (see Fig. 1.1). When a laser beam is moved around, the particles typically remain trapped in the beam and follow its movement.

There have been various explanations proposed as the responsible mechanism for this phenomenon. These will be discussed and in many cases dismissed in the sections that follow. We should note that the phenomenon described here is not a standard "optical tweezers" effect. Standard optical tweezers utilizes transparent particles,

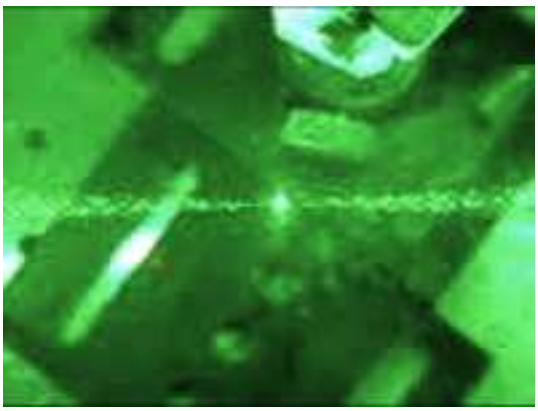

**Figure 1.1** An example of a levitated particle

which act as a sort of lens on the beam that goes through it, deflecting the direction of the light as it tries to leave the focus. As the light's direction is changed, so is its momentum, which places a restoring force on the particle.

The behavior in the trapping of opaque particles in a laser is counterintuitive when considering an exchange of momentum with the light field, since one would expect the photon pressure to "push" the particles out of the beam.

## 1.2 Influence of Ambient Pressure, Gravity, and Beam Roughness

BYU undergraduates studying the levitation of small, opaque particles have done much experimental work. They have observed particles that stay in the beam for up to eight hours (at which point the laser was turned off). In various experiments [8,9], it has been shown that a surrounding gas such as air is required. Levitation has been observed at pressures varying from a few torr to several atmospheres. The requirement of a surrounding gas indicates that the phenomenon is due to a radiometric effect, where the particle becomes heated and interacts with the surrounding air.

The phenomenon has been observed to be independent of gravity. This principle was confirmed in an experiment carried out on a NASA DC9 jet, where zero-gravity conditions were created for approximately 30 seconds at a time. [10] Particles were still observed to become and stay trapped. This gravity-independence rules out buoyancy of locally heated air as being responsible for the trapping.

Since opaque particles seem like they should be intensity-fleeing, it has been proposed that roughness of the laser beam could cause small pockets of low intensity that might coral an intensity-fleeing particle within a laser beam. However, an experiment was carried out in which the beam has been made sufficiently smooth to rule out this explanation as well. [11]

Thus, buoyancy and small pockets of low intensity have been ruled out as a mechanism for the stable trapping of opaque particles. Also, trapping works regardless of which way the laser is pointed, and gravity plays little or no role.

## 1.3 Overview

It is somewhat of a puzzle as to how the particle can become stably trapped in the laser focus. Ambient gas pressure is required, so it appears that the heating of the particle imparts energy to the surrounding gas molecules, and the recoil of many molecules apparently provides the force needed for levitation. One would expect the "sunny" side to become hotter, and therefore added recoil of molecules from that side would propel the particle out of the laser beam.

The basis for my thesis project is to investigate a hypothesis, which we call "shady-side heating." The basic question is whether there could be more heating on the side of the particle opposite the direction of the beam. In other words, could there be more light energy absorbed on the "shady side" of tiny particles? If so, the heating

from this excess absorbed energy could provide a mechanism for the stable trapping of small particles.

To test this hypothesis, we make the simplifying assumption that the trapped particles are spherical. The generally used and accepted theory for calculating electromagnetic fields incident on a spherical particle is Mie theory, developed by Gustav Mie in 1908 [12] and independently by others, including Lorenz. It is more general than the widely-known Rayleigh scattering in that all possible ratios of diameter to wavelength are treated. The solution is developed by splitting the waves into components with a radial electric component but no radial magnetic component (an electric wave) and vice versa (a magnetic wave). Maxwell's equations are put into spherical coordinates, and boundary conditions are applied at the sphere's surface. In this way, the equations for the electric and magnetic wave vectors can be found. Debye potentials are used as a way to derive these vector fields from a scalar potential.

Usually, Mie theory is used to find information about the scattered wave (see e.g. [12, 13, 14]). It is used extensively in meteorology when discussing such things as liquid droplets and dust in the air. Astronomers also use it in analyzing clouds of dust through which light shines (e.g. [15]). It also can be used in the characterization of particles, but once again it is the scattered wave that is typically of interest. There has been interesting work done by Dieter Bauer (to whom we are endebted for his help with Mie theory and coding) et al. in using Mie theory to discuss laser-illuminated electron bunches. [2]

Our approach is somewhat off the beaten path, in that we are interested in the absorbed field rather than the scattered field. There has been some work done in this vein (e.g. [16, 17]). It is important to note that a mechanism similar to that which we call shady-side heating has been proposed before. In a 1983 paper by Pluchino on opaque particle levitation [3], he proposed and analyzed such a mechanism involving

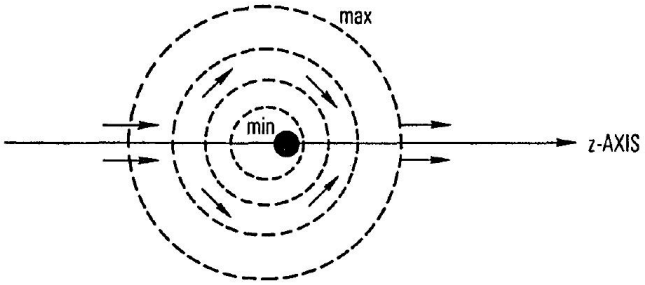


**Figure 1.2** Schematic representation of mechanism responsible for trapping a particle. Fig. 10 from Pluchino (1983).

the Poynting vector. The basic idea of his proposed mechanism is that the particle causes currents in the Poynting vector that cause it to have a higher value on the back side of the particle. The energy flow characterized by the Poynting vector has areas where it flows back towards the particle. Pluchino states, "The photons do not have to be directed back toward the source; it is only important that the rear half absorb more energy. Removal of this energy by the surrounding gas molecules imparts a force on the particle which is considerably greater than that due to photon momentum and is directed normal to the surface." A diagram of his proposed method is included in Fig. 1.2.

Our approach is thus to find expressions for the fields using Mie theory. In this thesis, I describe the Mie solutions inside a particle and present simulations of field distributions for particles ranging in size from less than a wavelength to 20 wavelengths. The results show that the notion of "shady-side" heating is not a plausible mechanism for describing radiometric particle levitation in an intense laser focus. The intuitive notion that the "sunny side" of the small sphere experiences a much stronger field and therefore higher absorption is correct.

# Chapter 2

# Calculations of Internal Mie Fields

## 2.1 Equations for the Internal Fields

The derivation of fields in the Mie regime is done in accordance with Born and Wolf [1] and is summarized in Appendix A. Treatments may also be found elsewhere, e.g. [13, 14, 18]. We consider the diffraction of a linearly polarized, monochromatic plane wave by a sphere of radius $a$, immersed in a homogeneous, isotropic medium, which for our purposes will ultimately be set to an index of one. Both the particle and the medium are assumed to be nonmagnetic. A schematic of the problem can be seen in Fig. 2.1. The internal electric field is given by:

$$\begin{cases} E_r^{(w)} = \frac{1}{k^{(II)^2}} \frac{\cos\varphi}{r^2} \sum_{l=1}^{\infty} l\,(l+1)\, {}^{e}A_l \psi_l \left(k^{(II)} r\right) P_l^{(1)}\left(\cos\theta\right) & (a) \\ E_\theta^{(w)} = -\frac{1}{k^{(II)}} \frac{\cos\varphi}{r} \sum_{l=1}^{\infty} \Big[ {}^{e}A_l \psi_l{}' \left(k^{(II)} r\right) P_l^{(1)'}\left(\cos\theta\right) \sin\theta \\ \qquad\qquad -i\ {}^{m}A_l \zeta_l^{(1)} \left(k^{(I)} r\right) P_l^{(1)}\left(\cos\theta\right) \frac{1}{\sin\theta} \Big] & (b) \\ E_\varphi^{(w)} = -\frac{1}{k^{(II)}} \frac{\sin\varphi}{r} \sum_{l=1}^{\infty} \Big[ {}^{e}A_l \psi_l{}' \left(k^{(II)} r\right) P_l^{(1)}\left(\cos\theta\right) \frac{1}{\sin\theta} \\ \qquad\qquad -i\ {}^{m}A_l \psi_l \left(k^{(II)} r\right) P_l^{(1)'}\left(\cos\theta\right) \sin\theta \Big] & (c) \end{cases} \tag{2.1}$$

Here, $\psi_l$ and $\zeta_l{}^{(1)}$ are Riccati-Bessel functions, which are discussed further in the next section. The $P_l^{(1)}$ are the associated Legendre polynomials of order one. $k^{(II)}$ is

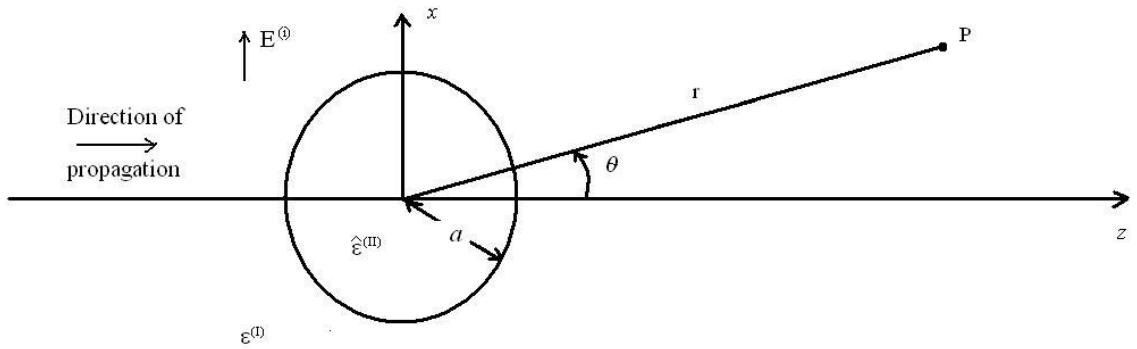


**Figure 2.1** Notation for the Mathematical Solution of the Mie Problem

the usual wave number inside the sphere defined by $k = \frac{n\omega}{c} = \sqrt{-k_1 k_2}$ where $k_1 \equiv \frac{i\omega n}{c}$ and $k_2 \equiv \frac{i\omega}{c}$. $n$ is the complex index of refraction $n = n_{re} + i\kappa$. The superscript $(II)$ denotes quantities associated with fields inside the sphere, while the superscript $(I)$ (which will appear later) denotes the region surrounding the sphere.

The characterizing $A$ coefficients are:

$$\begin{cases} {}^{e}A_l = i^{l-1}\frac{2l+1}{l(l+1)}\dfrac{\psi_l{}'\left(k^{(I)}a\right)\zeta_l^{(1)}\left(k^{(I)}a\right)-\psi_l\left(k^{(I)}a\right)\zeta_l^{(1)}{}'\left(k^{(I)}a\right)}{\frac{k^{(I)}}{k^{(II)}}\psi_l{}'\left(k^{(II)}a\right)\zeta_l^{(1)}\left(k^{(I)}a\right)-\frac{k_2^{(I)}}{k_2^{(II)}}\psi_l\left(k^{(II)}a\right)\zeta_l^{(1)}{}'\left(k^{(I)}a\right)} & (a) \\ {}^{m}A_l = i^{l-1}\frac{2l+1}{l(l+1)}\dfrac{\psi_l{}'\left(k^{(I)}a\right)\zeta_l^{(1)}\left(k^{(I)}a\right)-\psi_l\left(k^{(I)}a\right)\zeta_l^{(1)}{}'\left(k^{(I)}a\right)}{\frac{k_2^{(I)}}{k_2^{(II)}}\psi_l{}'\left(k^{(II)}a\right)\zeta_l^{(1)}\left(k^{(I)}a\right)-\frac{k^{(I)}}{k^{(II)}}\psi_l\left(k^{(II)}a\right)\zeta_l^{(1)}{}'\left(k^{(I)}a\right)} & (b) \end{cases} \tag{2.2}$$

These come from the relations:

$$\begin{cases} {}^{e}B_l\frac{1}{k^{(I)}}\zeta_l^{(1)}{}'\left(k^{(I)}a\right)+\frac{1}{k^{(I)}}i^{l-1}\frac{(2l+1)}{l(l+1)}\psi_l{}'\left(k^{(I)}a\right)=\frac{1}{k^{(II)}}{}^{e}A_l\psi_l{}'\left(k^{(II)}a\right) & (a) \\ {}^{m}B_l\frac{1}{k_2^{(I)}}\zeta_l^{(1)}{}'\left(k^{(I)}a\right)+\frac{1}{k_2^{(I)}}i^{l-1}\frac{(2l+1)}{l(l+1)}\psi_l{}'\left(k^{(I)}a\right)=\frac{1}{k_2^{(II)}}{}^{m}A_l\psi_l{}'\left(k^{(II)}a\right) & (b) \\ {}^{e}B_l\frac{1}{k_2^{(I)}}\zeta_l^{(1)}\left(k^{(I)}a\right)+\frac{1}{k_2^{(I)}}i^{l-1}\frac{(2l+1)}{l(l+1)}\psi_l\left(k^{(I)}a\right)=\frac{1}{k_2^{(II)}}{}^{e}A_l\psi_l\left(k^{(II)}a\right) & (c) \\ {}^{m}B_l\frac{1}{k^{(I)}}\zeta_l^{(1)}\left(k^{(I)}a\right)+\frac{1}{k^{(I)}}i^{l-1}\frac{(2l+1)}{l(l+1)}\psi_l\left(k^{(I)}a\right)=\frac{1}{k^{(II)}}{}^{m}A_l\psi_l\left(k^{(II)}a\right) & (d) \end{cases} \tag{2.3}$$

which come directly from detailed boundary conditions, (see Appendix A)

From an inspection of Eq. (2.1), one might think that there is a problem with the $\frac{1}{r}$ dependence at the origin, but the limit as $r \to 0$ is well-defined.

## 2.2 The Riccati-Bessel Functions and the Legendre Polynomials

In the expressions for the internal field, Eqs. (2.1)–(2.2), we may see that we must have relations for the Riccati-Bessel functions $\psi_l$ and ${\zeta_l}^{(1)}$, the Legendre polynomials of the first order $P_l^{(1)}$ and their derivatives. The primes indicate differentiation with respect to the arguments.

The definitions of $\psi_l$ and ${\zeta_l}^{(1)}$ are as follows: (see Appendix A):

$$\psi_l(\rho) = \sqrt{\tfrac{\pi\rho}{2}}\, J_{l+\frac{1}{2}}(\rho), \quad {\zeta_l}^{(1)}(\rho) = \sqrt{\tfrac{\pi\rho}{2}}\, H_{l+\frac{1}{2}}(\rho) \tag{2.4}$$

For the Riccati-Bessel functions, the following relation concerning derivatives of all types of Bessel functions is useful. Here, $\eta$ can represent any of these ($J$, $N$, or $H$):

$$\eta_l'(\rho) = \frac{1}{2}\left[\eta_{l-1}(\rho) - \eta_{l+1}(\rho)\right] \tag{2.5}$$

This implies:

$$\psi_l'(\rho) = \frac{1}{2}\left\{\sqrt{\frac{\pi\rho}{2}}\left[J_{l-1/2}(\rho) - J_{l+3/2}(\rho)\right] + \sqrt{\frac{\pi}{2\rho}}\, J_{l+1/2}(\rho)\right\} \tag{2.6}$$

$${\zeta_l^{(1)}}'(\rho) = \frac{1}{2}\left\{\sqrt{\frac{\pi\rho}{2}}\left[H_{l-1/2}(\rho) - H_{l+3/2}(\rho)\right] + \sqrt{\frac{\pi}{2\rho}}\, H_{l+1/2}(\rho)\right\} \tag{2.7}$$

As for the derivative of the associated Legendre polynomials, we use the following relation:

$$\left(x^2-1\right) P_l^{m\prime}(x) = lxP_l^m(x) - (l+m)\, P_{l-1}^m(x) \tag{2.8}$$

In our case of $m = 1$, we have:

$${P_l^{(1)}}'(x) = \frac{1}{(x^2-1)}\left[lxP_l^{(1)}(x) - (l+1)\, P_{l-1}^{(1)}(x)\right] \tag{2.9}$$

This obviously has a singularity when $x = 1$. Since, in our equations, $x = \cos\theta$, this problem occurs at the poles as defined in spherical coordinates. However, the limit

of the expression as $\cos\theta \to 0$ is well-defined, but must be treated carefully in the numerics.

Fortunately, MATLAB has functions for Bessel and Hankel functions (`besselj` and `besselh`) as well as Legendre polynomials (`legendre`).

## 2.3 Computation

The computation of the Mie fields are done using MATLAB. I have written a program that evaluates these fields at each point interior to the sphere near the surface. Additional information regarding my program and subroutines are provided in Appendix B. The infinite summations obviously must be truncated at some point. In accordance with Bohren and Huffman [14], we take the number of terms as:

$$l_{max} = s + 4s^{\frac{1}{3}} + 2 \tag{2.10}$$

where $s$ is the size parameter $s \equiv k^{(I)}a$. One may see how this converges and how appropriate this is by looking at the values of the absorption parameters (the $A$'s) as $l$ increases, which is done in Fig. 2.2 for an aluminum sphere with radius 10 times the wavelength. In this case, $l_{max} = 81$.

Once the components of the complex field have been computed, the MATLAB code I developed computes the magnitude of $\overrightarrow{E}^* \cdot \overrightarrow{E}$. This quantity is proportional to the time-averaged intensity and, for simplicity, will hereafter be referred to as intensity. Since the absorbed energy is directly related to intensity, we may characterize the energy absorption distribution by characterizing this intensity distribution.

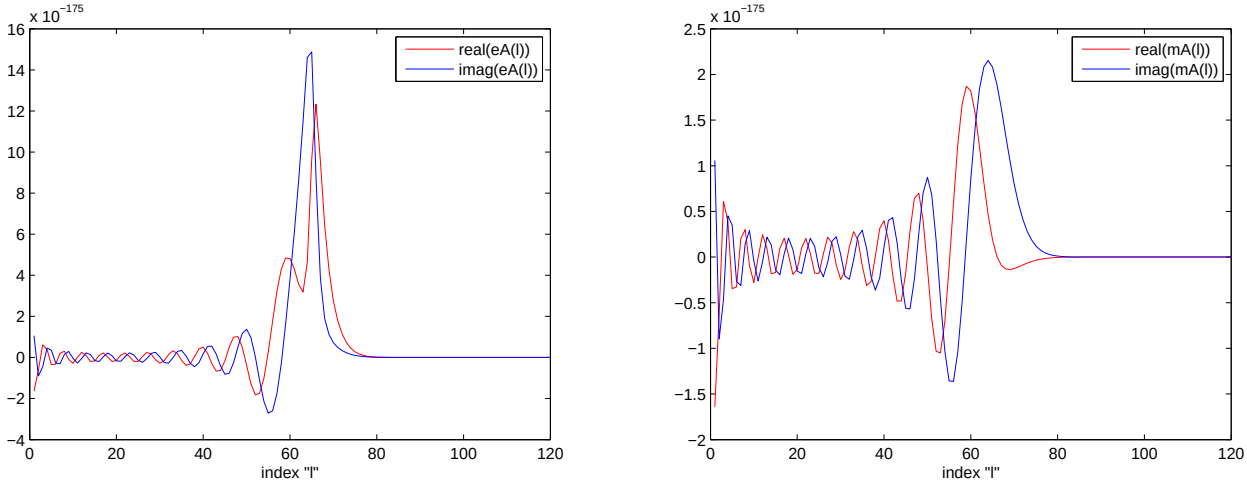


**Figure 2.2** Values of the absorption parameters ${}^{e}A_l$ and ${}^{e}A_l$ for an aluminum sphere with $a = 10\lambda$ ($l_{max} = 81$)

# Chapter 3

# Results

## 3.1 Fields within a Mie Sphere

In this chapter we examine the energy absorption distributions in various spheres. Because many materials of interest have small skin depth at our wavelength, we concentrate on the regions inside the sphere near the surface.

It is obviously essential to specify the optical constants of the materials in question. These have been obtained from Palik [19]. Calculations are carried out for aluminum, graphite, silver, and tungsten, which have all been observed to levitate in a laser in our laboratory. The values of the complex index of refraction for $\lambda = 532$nm, where $n_{re}$ is the real part and $\kappa$ is the imaginary part (i.e. the absorption coefficient), are provided in Table 3.1.

| | $n_{re}$ | $\kappa$ |
|---|---|---|
| Aluminum | 0.912 | 6.55 |
| Graphite (e) | 2.03 | 0.64 |
| Graphite (o) | 2.67 | 1.34 |
| Silver | 0.129 | 3.25 |
| Tungsten | 3.50 | 2.72 |

**Table 3.1** Complex Indices

We plot the surface of the sphere showing the amount of absorbed energy just inside of the sphere. We use fifty points on the surface of the sphere for our plots of the absorption. We also plot the entire field, inside and out, for a two-dimensional cross section in the x-z plane. Twenty-five grid points are used for each spatial unit of the sphere's radius $a$ in our plots of the complete field.

## 3.2 Absorption within a Mie Sphere

Fig. 3.1 shows plots of the intensity for a graphite particle in a laser field. Our plots of the internal intensity show first the "shady" side of the sphere, and then the "sunny" side, as dictated by our choice of the positive z-direction as the direction of the light propagation. We run calculations for $a = 5\lambda$, which with our wavelength of 532 nm, corresponds to a $\sim$5 µm diameter particle. The only things that matter in the calculations are the ratio of particle radius to wavelength and the refractive index at the pertinent wavelength. From this plot, we may see that there is not any shady-side heating under these conditions.

To further understand what is happening, we have plotted the complete field in Fig. 3.2. This necessitates calculation of the incident and scattered fields, details of which can be found in Appendix A. These plots, which begin on the next page, show

the $\overrightarrow{E}^* \cdot \overrightarrow{E}$ intensity. All plots are shown in units of the sphere's radius, $a$.

### 3.2.1 $a = 5\lambda$

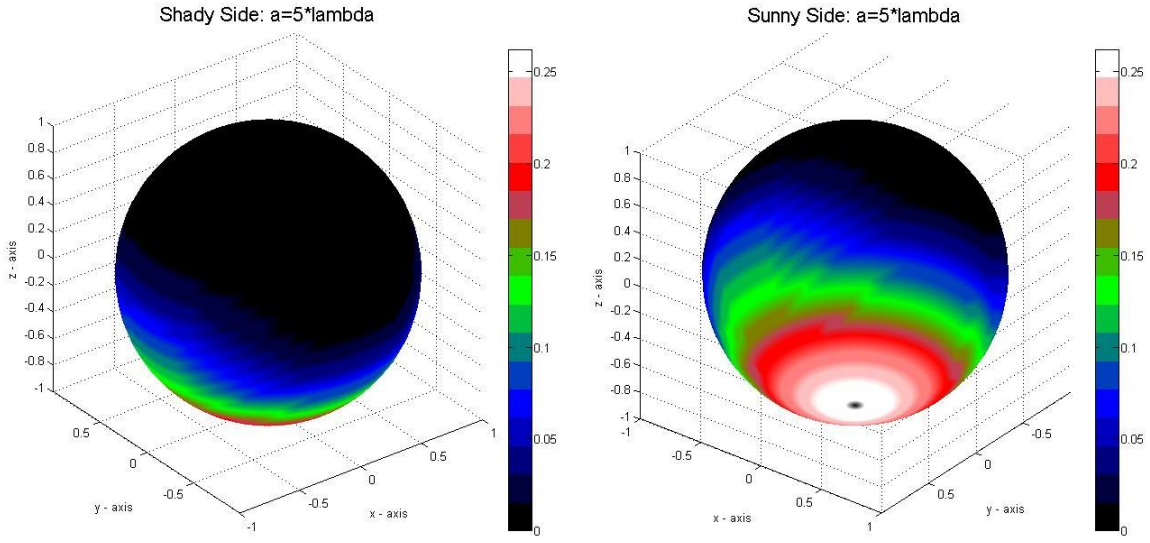


**Figure 3.1** Internal absorption at the surface of a sphere with $a = 5\lambda$. The beam propagates from bottom to top.

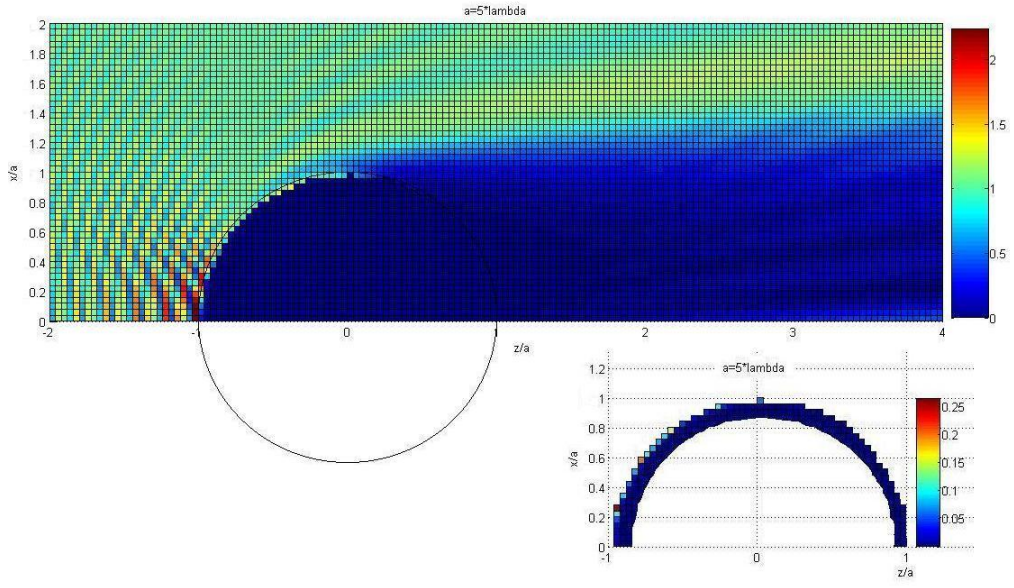


**Figure 3.2** Complete field for a ∼5 µm diameter particle ($a = 5\lambda$). The beam propagates from left to right.

From our calculations, we see no counterintuitive effects. It seems that the particles gets "blasted" on the sunny side, and that the shady side receives little intensity at all. There is a "void" cleared out behind the particle as well, so there is no striking curling of fields behind the particle that could cause an increase of absorption on that side, as posited by Pluchino. [3]

## 3.3 Size Dependence

For a larger particle (with $a = 10\lambda$), as seen in Figs. 3.3 and 3.4, we can see that the field gets even weaker on the back side. The results for smaller particles are shown beginning in Figs. 3.5–3.14. Even for submicron particles, there is very little shady-side heating. It seems that all of the particles receive a lot more intensity on the side of the particle facing the beam.

### 3.3.1 $a = 10\lambda$

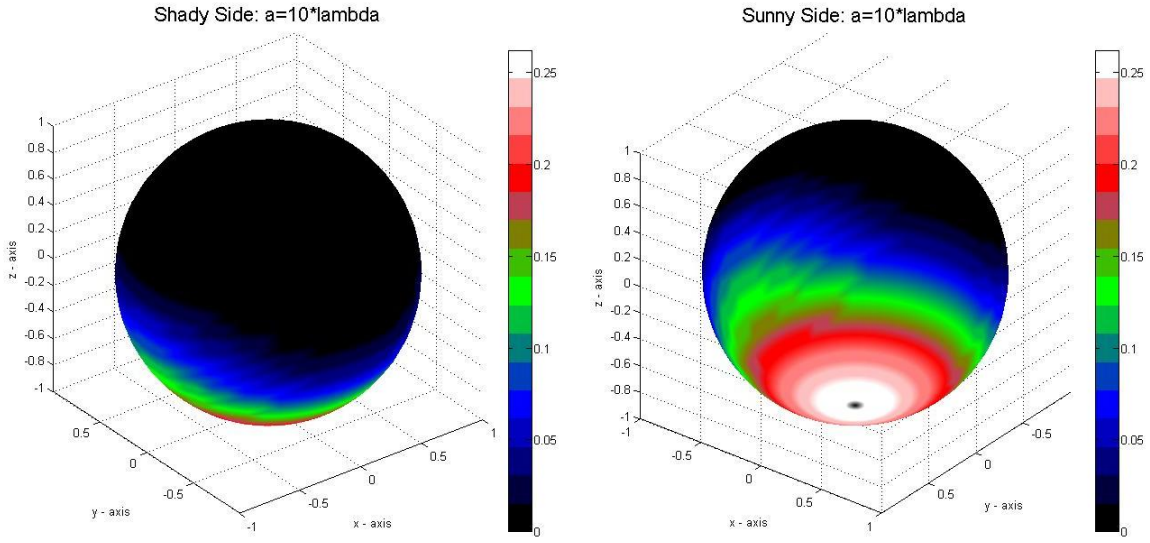


**Figure 3.3** Internal absorption at the surface of a sphere with $a = 10\lambda$. The beam propagates from bottom to top.

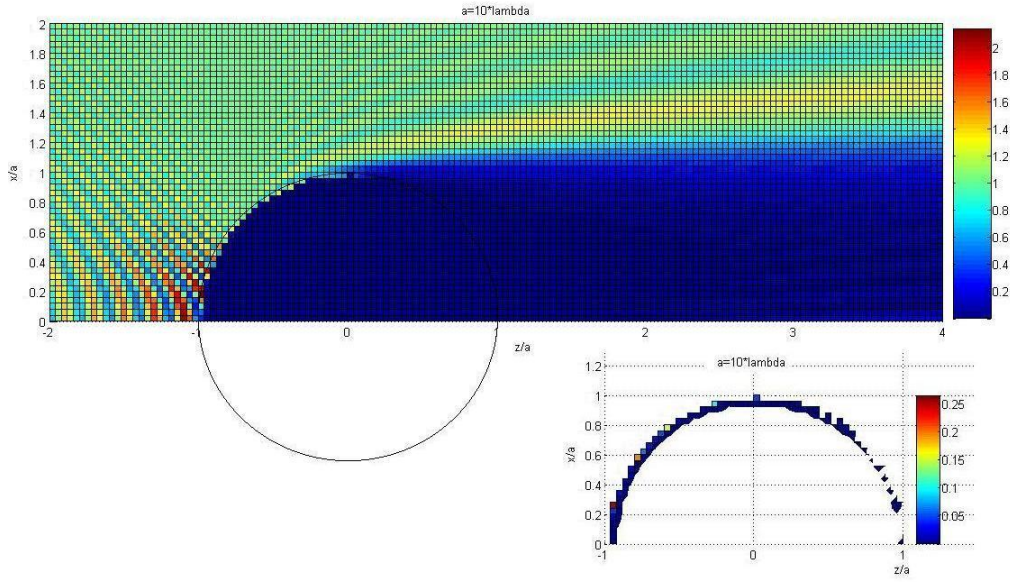


**Figure 3.4** Complete field for $a = 10\lambda$. The beam propagates from left to right.

### 3.3.2 $a = 2\lambda$

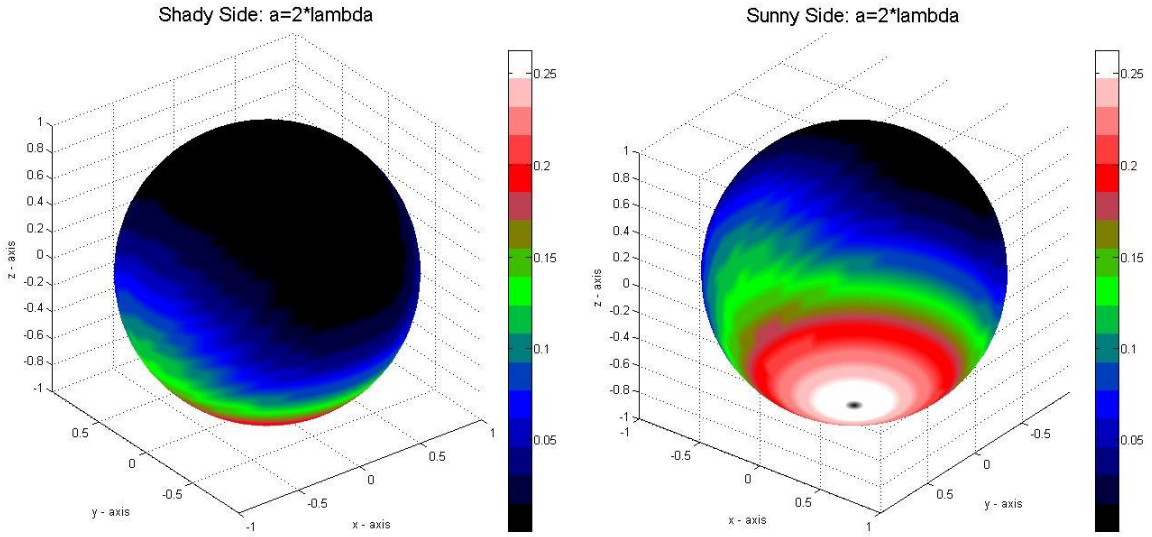


**Figure 3.5** Internal absorption at the surface of a sphere with $a = 2\lambda$. The beam propagates from bottom to top.

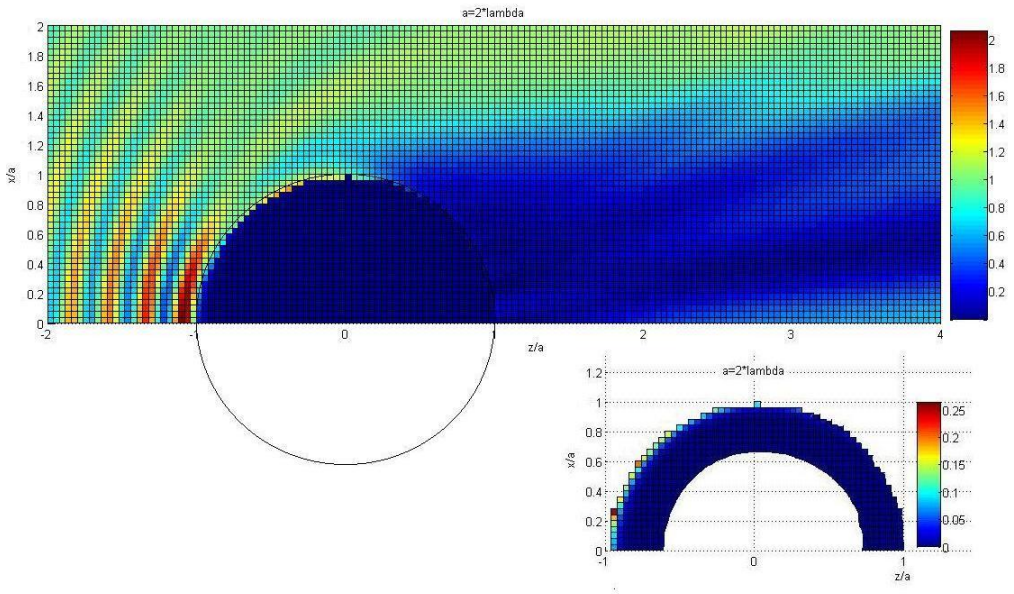


**Figure 3.6** Complete field for a $a = 2\lambda$. The beam propagates from left to right.

### 3.3.3 $a = \lambda$

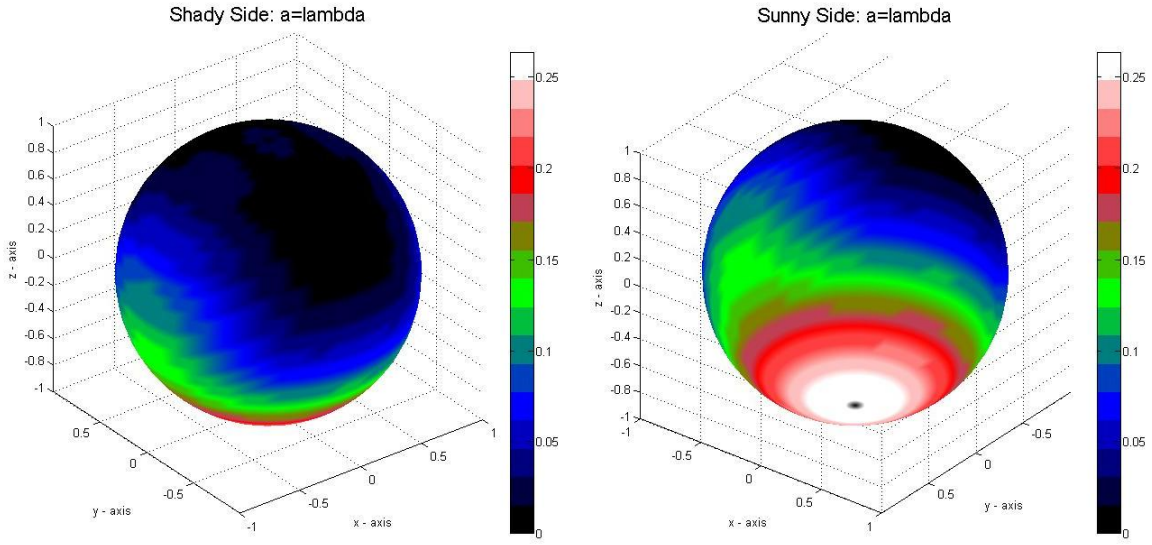


**Figure 3.7** Internal absorption at the surface of a sphere with $a = \lambda$. The beam propagates from bottom to top.

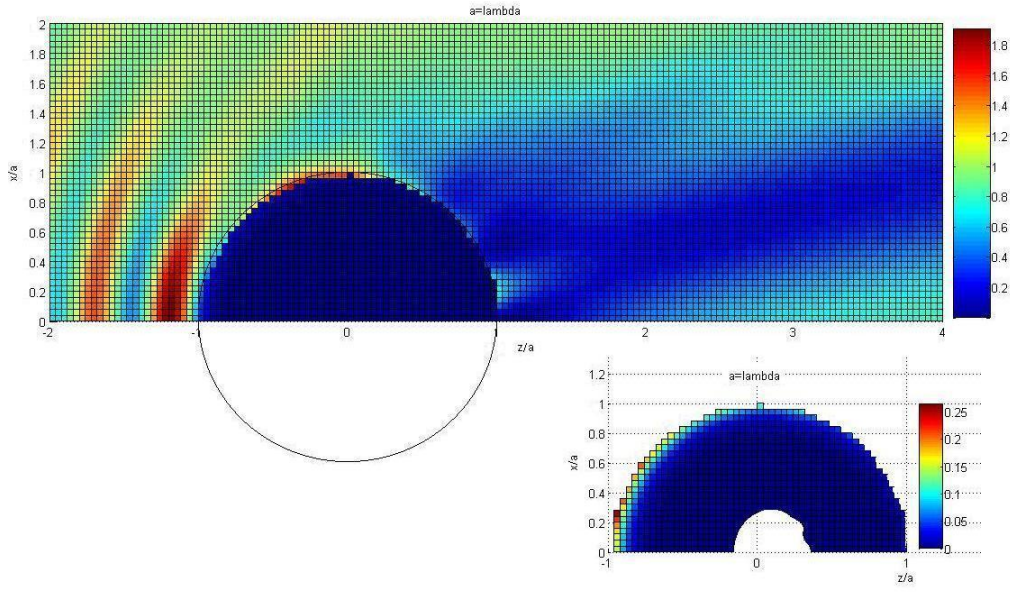


**Figure 3.8** Complete field for $a = \lambda$. The beam propagates from left to right.

### 3.3.4 $a = \lambda/2$

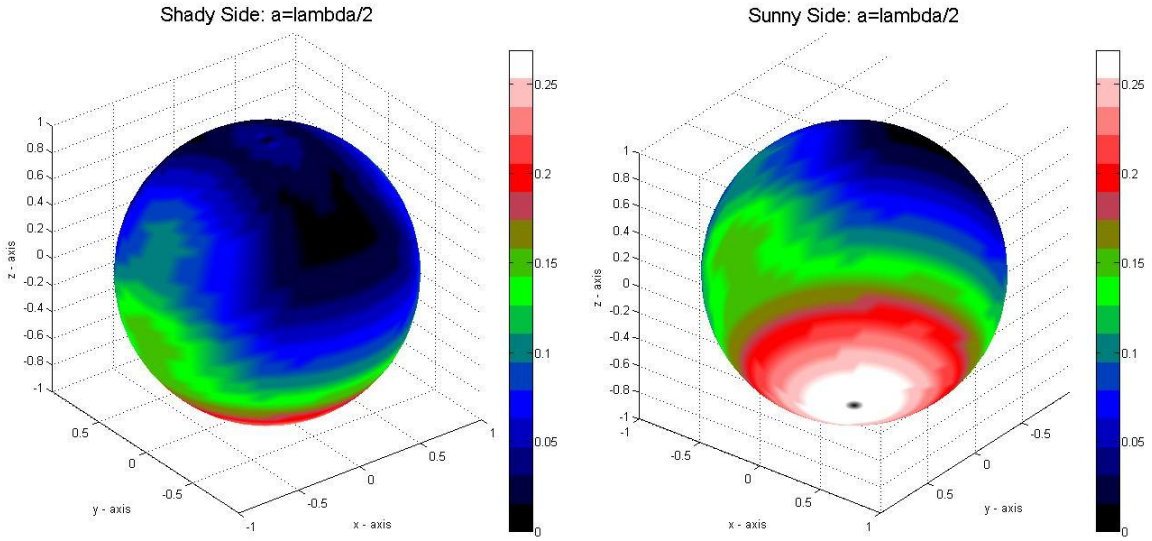


**Figure 3.9** Internal absorption at the surface of a sphere with $a = \lambda/2$. The beam propagates from bottom to top.

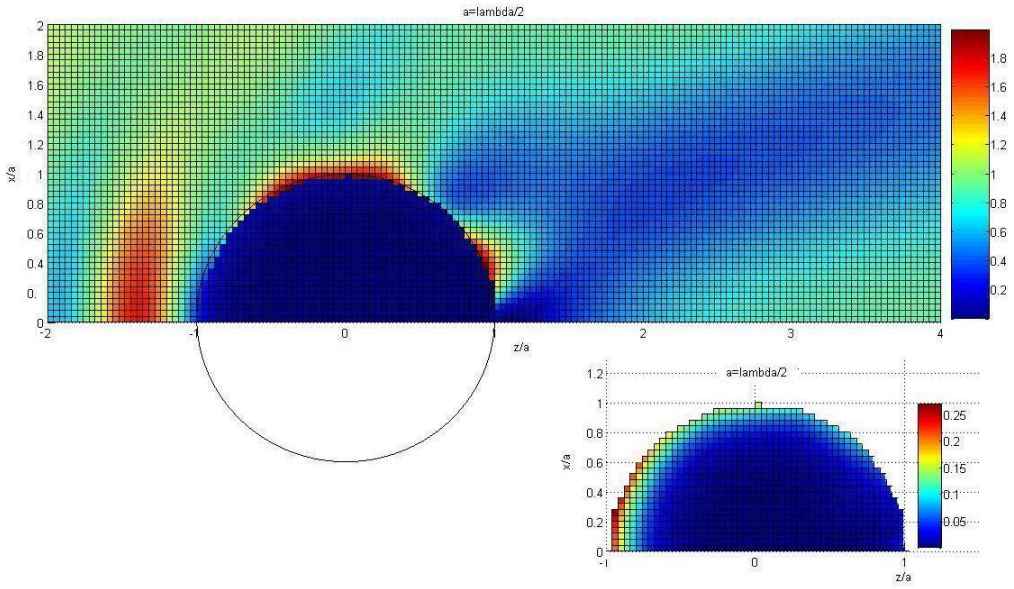


**Figure 3.10** Complete field for $a = \lambda/2$. The beam propagates from left to right.

### 3.3.5 $a = \lambda/5$

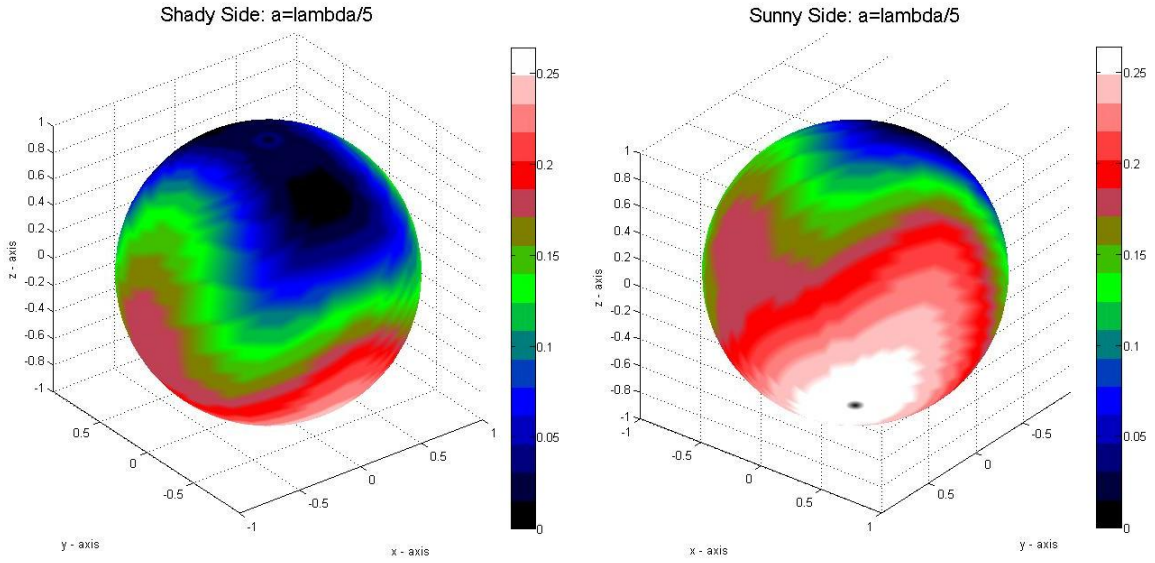


**Figure 3.11** Internal absorption at the surface of a sphere with $a = \lambda/5$. The beam propagates from bottom to top.

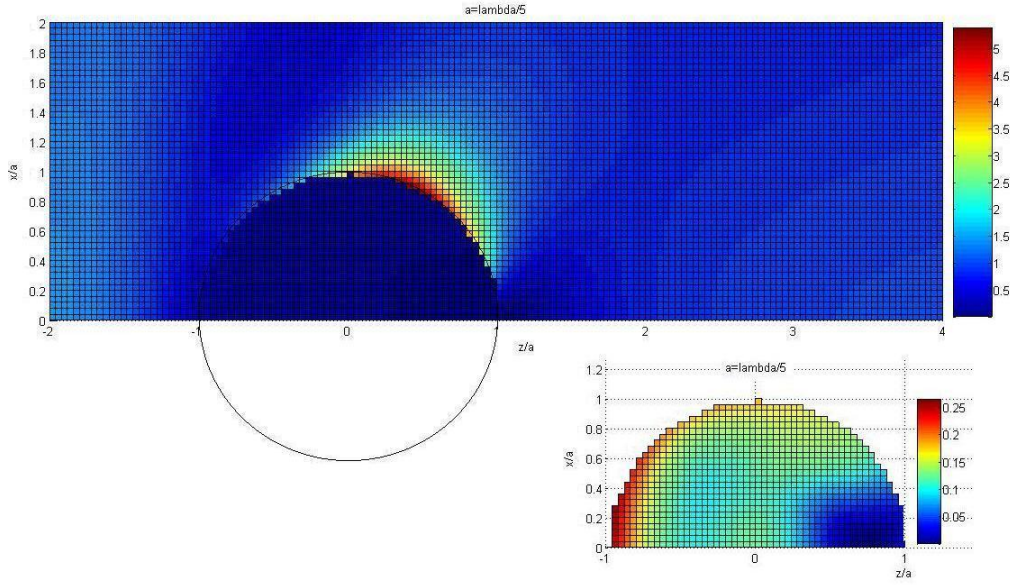


**Figure 3.12** Complete field for $a = \lambda/5$. The beam propagates from left to right.

### 3.3.6 $a = \lambda/10$

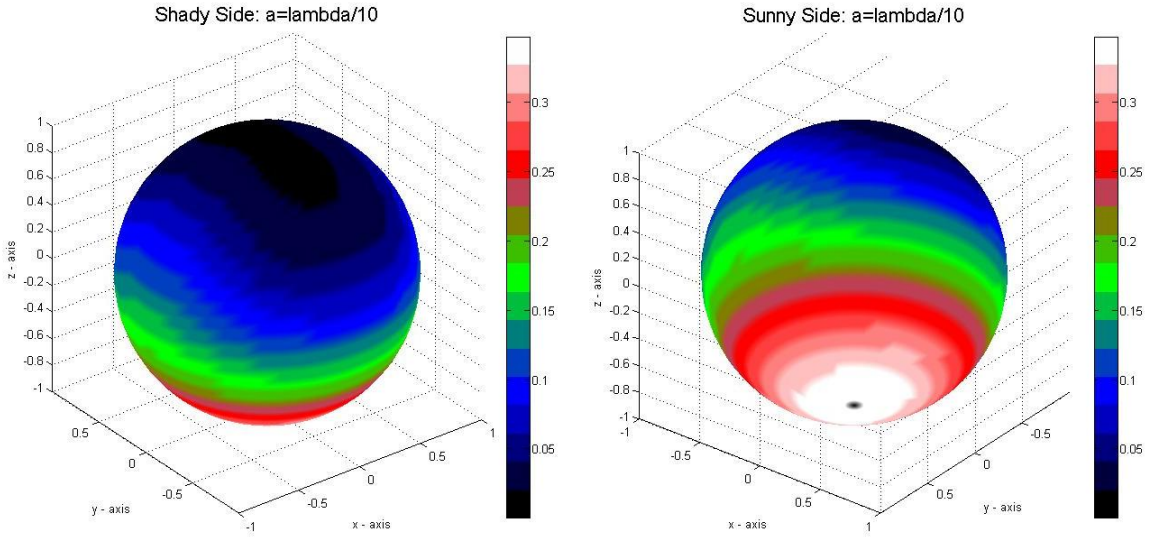


**Figure 3.13** Internal absorption at the surface of a sphere with $a = \lambda/10$. The beam propagates from bottom to top.

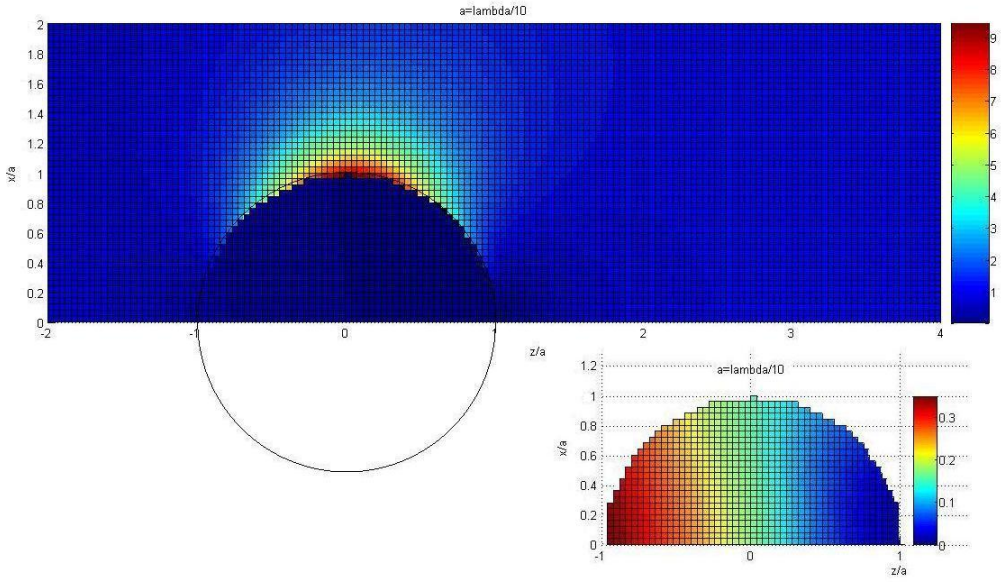


**Figure 3.14** Complete field for $a = \lambda/10$. The beam propagates from left to right.

## 3.4 Investigation of Possible Resonances

The particle sizes we have investigated so far do not experience shady-side heating. However, in observing the internal intensity distributions for the particle sizes $a = \lambda$ (corresponding to a $\sim$1 µm diameter particle), $a = \lambda/2$ (532nm=.532 µm diameter), $a = \lambda/5$ (.2 µm diameter), and $a = \lambda/10$ ($\sim$.05 µm diameter), an effect is noticed which merits further investigation.

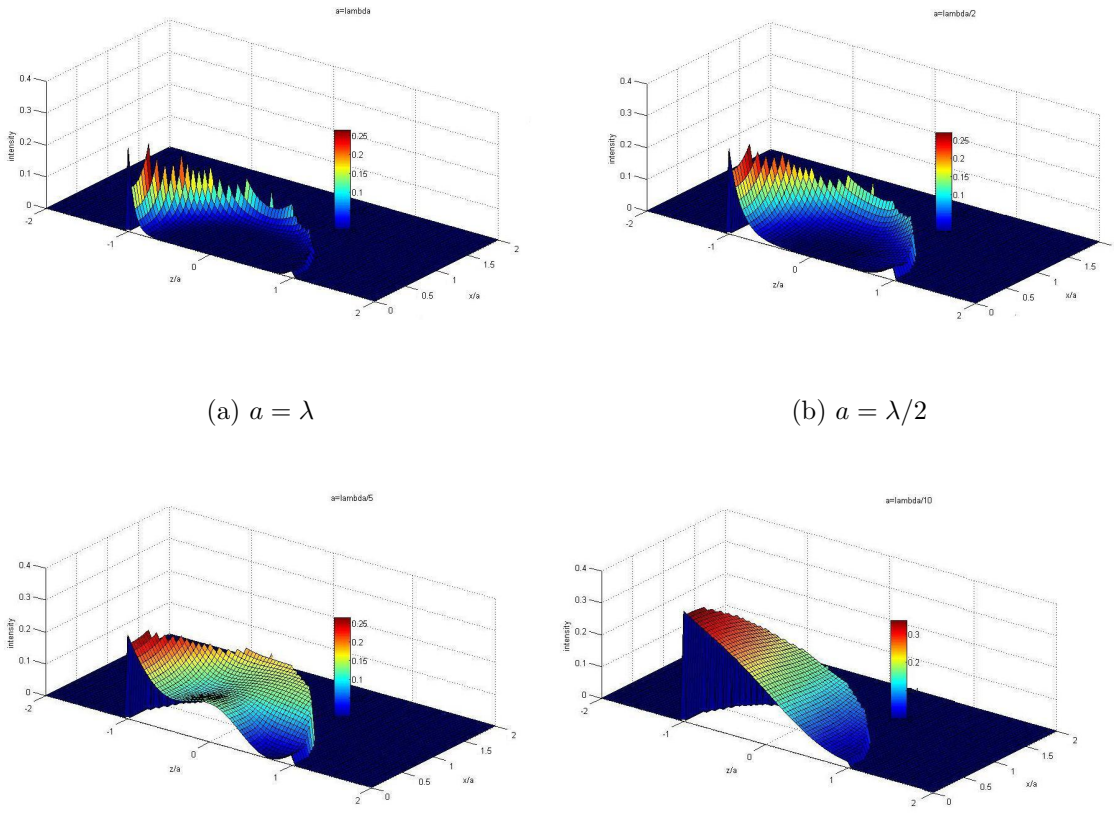


(a) $a = \lambda$ (b) $a = \lambda/2$

(c) $a = \lambda/5$ (d) $a = \lambda/10$

**Figure 3.15** Internal absorption with possible hints of resonances.

In Fig. 3.15, the magnitude of the intensity is represented by height. When $a = \lambda$, the absorption on the sunny side is much more than that on the shady side (it's

"higher" on the sunny side than on the shady side). When $a = 2\lambda$, the difference in height between front and back is not as much. In fact, there are pockets of higher absorption on the shady side corresponding to places where the external field regions of high intensity "curl around" to the shady side, as can be seen from Fig. 3.10. When $a = 5\lambda$, there is even more curling (See Fig. 3.12), and there are places in the middle of the sphere where the height is greater than corresponding x-values closer to the sunny side. This "bump", which can be seen in Fig. 3.15(c), is gone at $a = \lambda/10$.

The question this brings up is whether, somewhere in this range of particle sizes, there might be some kind of resonance that could make it so the magnitude of the intensities on both sides are equal or even higher on the shady side. This would give an explanation of the phenomenon of stable particle trapping and would be consistent with the fact that the particles are self-selecting when they become trapped. I investigated the solutions from $a = \lambda$ to $a = 10\lambda$ in small steps to see if any such resonances might exist.

To investigate this, I calculated what I call the "Center of Intensity" in the z-direction.

$$R_I = \frac{\sum z_n I_n}{\sum I_n} \tag{3.1}$$

The closer the center of intensity is to the shady side of the sphere (positive z-direction), the more of a shady-side heating effect we have. I first plotted this quantity from $a = 10\lambda$ (corresponding to $\lambda/a = 0.1$ on the figure) to $a = \lambda/10$ in increments of $\lambda/a = 0.1$ (see Fig. 3.16(a)).

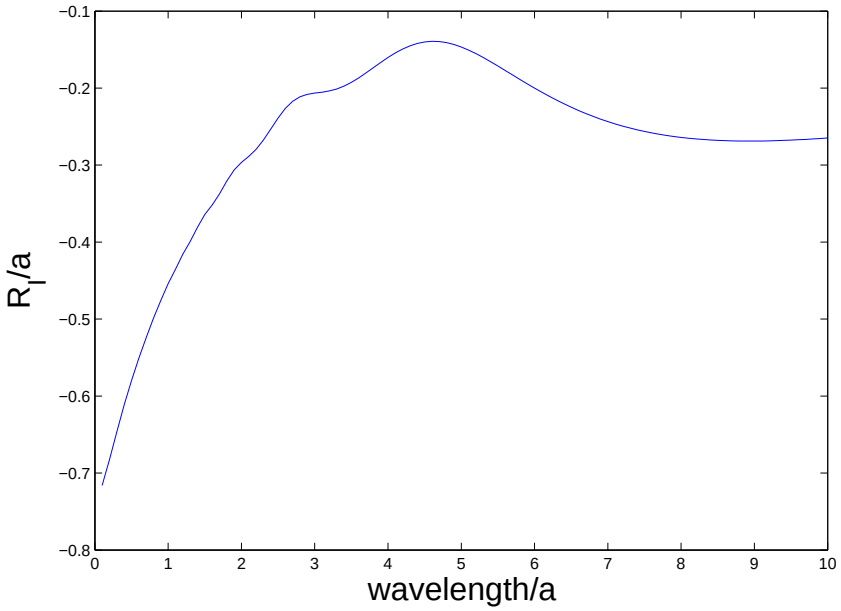


**Figure 3.16** Center of intensity as a function of particle size. Negative numbers for $R_I/a$ indicate a center of intensity further to the sunny side than the center of the sphere.

Note that for the sizes of particles we're interested in, $a = 10\lambda$ (corresponding to $\lambda/a = .1$) to $a = \lambda$ (corresponding to $\lambda/a = 1$), the center of intensity is well on the sunny side of the sphere.

To make sure I hadn't missed any resonances in the sizes where the interesting effects are happening, I repeated the calculations from $a = \lambda$ to $a = \lambda/5$ in increments of $\lambda/a = 0.01$, with the same result. The furthest toward the shady side that this center of intensity got was $R_I = -0.14a$ at $a = \lambda/4.62$. Plots of the intensity distribution for this particle size are included in Fig. 3.17.

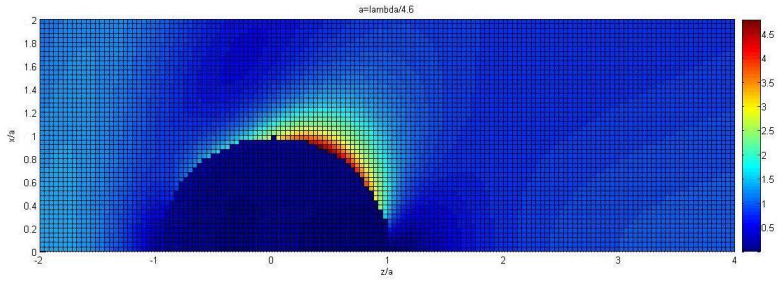


(a) $a = \lambda/4.6$ external

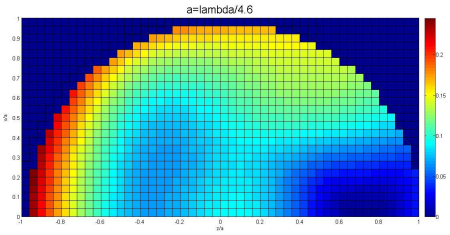


(b) $a = \lambda/4.6$ internal

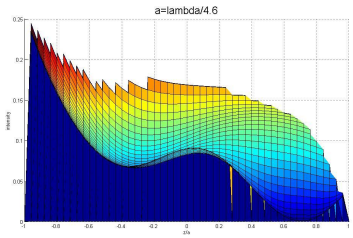


(c) $a = \lambda/4.6$ internal height

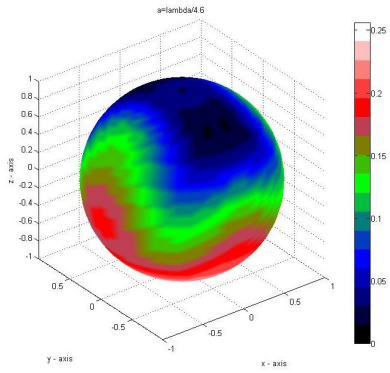


(d) $a = \lambda/4.6$ shady side

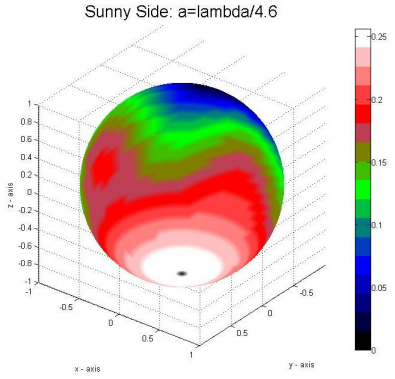


(e) $a = \lambda/4.6$ sunny side

**Figure 3.17** Intensity distribution for $a = \lambda/4.6$, where $R_I$ is furthest toward the shady side.

One might say that there is a sort of shady-side heating for sub-wavelength-size particles, but these are much smaller than the ones we have observed to become trapped in the laser. When the external field "wraps around" to the back side of the particle, it heats up the sphere on the back side. However, the particle still receives more intensity on the sunny side, so this mechanism cannot explain the stable particle trapping.

## 3.5 Conclusions

Our hypothesis of shady-side heating does not appear to be the mechanism responsible for the observed small-particle levitation. Our results show that, even though there are some times when the shady side does absorb, all of the particles absorb much more on the sunny side, especially when they are larger, such as five or ten microns. Some other mechanism will need to be proposed in order to explain the stability of the phenomenon.

Some ideas for responsible mechanisms still include a kind of shady-side heating, associated with unusual particle geometries, since particles that become trapped are self-selected as a powder is sprinkled through the laser focus. There could also be some kind of tumbling effect that causes the heated part of the sphere to rotate around to the shady side.

Perhaps understanding of the process must be sought through a study of the molecular flow range dynamics of gases. Since it has been observed that a gaseous medium is needed for the phenomenon to occur, movement of the gases around the particle might be the key to explaining the levitation. Investigating such things as circularly or elliptically polarized light might help us to further understand the mechanism.

# Bibliography


[1] M. Born and E. Wolf, *Principles of Light and Optics*, 7th ed. (Cambridge University Press, Cambridge, UK, 1999), pp. 759–789.

[2] T. Liseykina, S. Pirner, and D. Bauer, "Relativistic Attosecond Electron Bunches from Laser-Illuminated Droplets," arXiv:0906.1142v1 [physics.plasm-ph] (2009).

[3] A. Pluchino, "Radiometric levitation of spherical carbon aerosol particles using a Nd:YAG laser," Applied Optics **22 (12),** 1861–1866 (1983).

[4] A. D. May, E. G. Rawson, and E. H. Hara, "Propulsion and Angular Stabilization of Dust Particles in a Laser Cavity," Journal of Applied Physics **38 (13),** 5290–5292 (1966).

[5] M. Lewittes, S. Arnold, and G. Oster, "Radiometric levitation of micron sized spheres," Appl. Phys. Lett. **40 (6),** 455–457 (1982).

[6] J. Huisken and E. H. K. Stelzer, "Optical levitation of absorbing particles with a nominally Gaussian laser beam," Optics Letters **27 (14),** 1223–1223 (2002).

[7] A. Hendrickson, "Radiometric levitation of opaque particles in a laser beam,", Senior Thesis, Brigham Young University, 2005.

[8] R. Lindsey, "Optical levitation of opaque particles in a laser beam at high and low pressures,", Senior Thesis, Brigham Young University, 2005.

[9] R. Petersen, "Radiometric particle levitation in a laser beam at high ambient gas pressure,", Senior Thesis, Brigham Young University, 2008.

[10] J. Painter, "Optical levitation of opaque particles in a laser beam: zero-gravity experiment,", Senior Thesis, Brigham Young University, 2004.

[11] M. Martin, "High-resolution imaging of a laser beam used to levitate opaque microscopic particles,", Senior Thesis, Brigham Young University, 2006.

[12] G. Mie, "Beitrge zur Optik trber Medien, speziell kolloidaler Metallsungen," Annalen der Physik **25 (1),** 377–445 (1908).

[13] H. C. van de Hulst, *Light Scattering By Small Particles* (Wiley, New York, 1957).

[14] C. F. Bohren and D. R. Huffman, *Absorption And Scattering Of Light By Small Particles* (Wiley, New York, 1983), pp. 82–129, 477.

[15] E. A. Margerum and V. Vand, "Light scattering by small graphite spheres," Monthly Notices of the Royal Astronomical Society **128,** 431–434 (1964).

[16] H. Suzuki and I.-Y. S. Lee, "Average energy flow of optical pulses in dispersive media," International Journal of Physical Sciences **3 (1),** 38–41 (2008).

[17] T. K. Nadejda Velesco and G. Schweiger, "Computation of the internal field of a large spherical particle by use of the geometrical-optics approximation," Applied Optics **36 (33),** 8724–8728 (1997).

[18] P. W. Barber and S. C. Hill, *Light Scattering by Particles: Computational Methods* (World Scientific, New Jersey, 1990), pp. 187–254.

[19] E. D. Palik, *Handbook of Optical Constants of Solids* (Elsevier, New York, 1998).

# Appendix A

# Solving for Internal Fields of Mie Particles

## A.1 Method

We follow the example of Born and Wolf [1] in considering the diffraction of a plane, linearly polarized, monochromatic wave by a sphere of radius $a$, immersed in a homogeneous, isotropic medium. Both the particle and the medium are nonmagnetic.

We apply Maxwell's equations in vector form and in spherical coordinates to obtain six coupled partial differential equations. In order to obtain a complete solution, we represent the solution of these equations in terms of two linearly independent fields, one with a radial electric component but no radial magnetic component (an electric wave) and one with a radial magnetic component but no radial electric component (a magnetic wave.) We then show that each wave may be derived by a scalar Debye potential, each of which satisfies the wave equation.

To solve this wave equation, we use separation of variables, which leads us to a series solution involving Bessel, Neumann, and Hankel functions as well as associ-

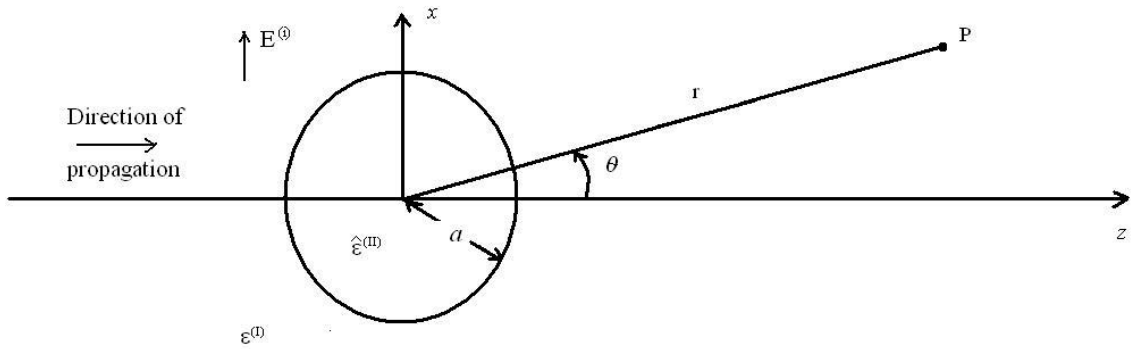


**Figure A.1** Notation for the Mathematical Solution of the Mie Problem

ated Legendre polynomials. The problem is thus reduced to finding the unknown coefficients for these series expansions. These are found by applying the boundary conditions at the surface of the sphere.

## A.2 General Equations

The notation used for the solution of this problem will be as follows: We have rectangular coordinates with the origin at the center of the sphere, the z-direction as the direction of propagation, and the x-direction as the direction of the wave's electric vector (remember that we have a linearly polarized plane wave). A superscript $I$ denotes quantities relating to the medium surrounding the sphere, while a superscript $II$ denotes those relating to the sphere itself. See Fig. A.1 for clarification.

We describe the wave at all points through Maxwell's equations:

$$\begin{cases} \nabla \cdot \overrightarrow{E} = 0 & (a) \\ \nabla \times \overrightarrow{E} = -\frac{\partial \overrightarrow{B}}{\partial t} & (b) \\ \nabla \cdot \overrightarrow{B} = 0 & (c) \\ \nabla \times \overrightarrow{B} = \mu_0 \varepsilon \frac{\partial \overrightarrow{E}}{\partial t} + \mu_0 \overrightarrow{J} & (d) \end{cases} \tag{A.1}$$

If we assume standard time independence $e^{-i\omega t}$ on both vectors, we can express

the two curl equations as follows:

$$\begin{cases} \nabla \times \overrightarrow{B} = -k_1 \overrightarrow{E} & (a) \\ \nabla \times \overrightarrow{E} = k_2 \overrightarrow{B} & (b) \end{cases} \tag{A.2}$$

where

$$\begin{cases} k_1 = \frac{i\omega n^2}{c} & (a) \\ k_2 = \frac{i\omega}{c} & (b) \end{cases} \tag{A.3}$$

Note that $k$ is the usual wave number and that $n(\omega)$ is the complex index so that:

$$k^2 = \frac{\omega^2}{c^2}(1+\chi) = -k_1 k_2 \quad and \quad n(\omega) \equiv \sqrt{1+\chi} \tag{A.4}$$

When we express these fields in spherical coordinates, we obtain:

$$\begin{cases} (a) \begin{cases} -k_1 E_r = \frac{1}{r^2 \sin\theta}\left[\frac{\partial}{\partial\theta}(rB_\varphi \sin\theta) - \frac{\partial}{\partial\varphi}(rB_\theta)\right] & (\alpha) \\ -k_1 E_\theta = \frac{1}{r\sin\theta}\left[\frac{\partial}{\partial\varphi}B_r - \frac{\partial}{\partial r}(rB_\varphi \sin\theta)\right] & (\beta) \\ -k_1 E_\varphi = \frac{1}{r}\left[\frac{\partial}{\partial r}(rB_\theta) - \frac{\partial}{\partial\theta}B_r\right] & (\gamma) \end{cases} \\ (b) \begin{cases} k_2 B_r = \frac{1}{r^2 \sin\theta}\left[\frac{\partial}{\partial\theta}(rE_\varphi \sin\theta) - \frac{\partial}{\partial\varphi}(rE_\theta)\right] & (\alpha) \\ k_2 B_\theta = \frac{1}{r\sin\theta}\left[\frac{\partial}{\partial\varphi}E_r - \frac{\partial}{\partial r}(rE_\varphi \sin\theta)\right] & (\beta) \\ k_2 B_\varphi = \frac{1}{r}\left[\frac{\partial}{\partial r}(rE_\theta) - \frac{\partial}{\partial\theta}E_r\right] & (\gamma) \end{cases} \end{cases} \tag{A.5}$$

We'll represent the solution of these equations in terms of two linearly independent fields as discussed above, which we will name $({}^eE\ ,\ {}^eB)$ and $({}^mE\ ,\ {}^mB)$, each of which will satisfy Eq. (A.5) such that:

$$(a) \quad {}^eE_r = E_r, \quad {}^eB_r = 0 \quad and \quad (b) \quad {}^mE_r = 0, \quad {}^mB_r = B_r \tag{A.6}$$

Under these constraints and the two Maxwell equations involving divergence, we can show that Maxwell's equations, i.e. Eq. (A.5), may be satisfied by using Debye potentials. This is an important point. It is analogous to to situation where, in Cartesian coordinates, we obtain a vector field from a scalar potential. Debye potentials

allow one to do the same thing in spherical coordinates. The complete solution to our set of equations is as follows:

$$\begin{cases} (a) \begin{cases} E_r = {}^eE_r + {}^mE_r = \frac{\partial^2}{\partial r^2}\left(r^e\Pi\right) + k^2 r^e\Pi & (\alpha) \\ E_\theta = {}^eE_\theta + {}^mE_\theta = \frac{1}{r}\,\frac{\partial^2}{\partial r\partial\theta}\left(r^e\Pi\right) + \frac{k_2}{r\sin\theta}\,\frac{\partial}{\partial\varphi}\left(r^m\Pi\right) & (\beta) \\ E_\varphi = {}^eE_\varphi + {}^mE_\varphi = \frac{1}{r\sin\theta}\,\frac{\partial^2}{\partial r\partial\varphi}\left(r^e\Pi\right) - \frac{k_2}{r}\,\frac{\partial}{\partial\theta}\left(r^m\Pi\right) & (\gamma) \end{cases} \\ (b) \begin{cases} B_r = {}^mB_r + {}^eB_r = \frac{\partial^2}{\partial r^2}\left(r^m\Pi\right) + k^2 r^m\Pi & (\alpha) \\ B_\theta = {}^mB_\theta + {}^eB_\theta = -\frac{k_1}{r\sin\theta}\,\frac{\partial}{\partial\varphi}\left(r^e\Pi\right) + \frac{1}{r}\,\frac{\partial^2}{\partial r\partial\theta}\left(r^m\Pi\right) & (\beta) \\ B_\varphi = {}^mB_\varphi + {}^eB_\varphi = \frac{k_1}{r}\,\frac{\partial}{\partial\theta}\left(r^e\Pi\right) + \frac{1}{r\sin\theta}\,\frac{\partial^2}{\partial r\partial\varphi}\left(r^m\Pi\right) & (\gamma) \end{cases} \end{cases} \tag{A.7}$$

where both potentials $r^e\Pi$ and $r^m\Pi$ are solutions of the wave equation:

$$\nabla^2\Pi + k^2\Pi = 0 \tag{A.8}$$

## A.3 Expansion of Solution

The method of separation of variables will be used to solve this partial differential equation, Eq. (A.8). We take:

$$\Pi = R\left(r\right)\Theta\left(\theta\right)\Phi\left(\varphi\right) \tag{A.9}$$

Upon plugging this into our wave equation, we obtain the following:

$$\begin{cases} \frac{\partial^2}{\partial r^2}\left(rR\right) + \left(k^2 - \frac{\alpha}{r^2}\right)rR = 0 & (a) \\ \frac{1}{\sin\theta}\,\frac{\partial}{\partial\theta}\left(\sin\theta\frac{\partial}{\partial\theta}\Theta\right) + \left(\alpha - \frac{\beta}{\sin^2\theta}\right)\Theta = 0 & (b) \\ \frac{\partial^2}{\partial\varphi^2}\Phi + \beta\Phi = 0 & (c) \end{cases} \tag{A.10}$$

The solutions of these three equations are:

$$rR = c_l\psi_l\left(kr\right) + d_l\chi_l\left(kr\right), \quad \Theta = P_l^m\left(\cos\theta\right), \quad \Phi = a_m\cos\left(m\phi\right) + b_m\sin\left(m\phi\right) \tag{A.11}$$

$\psi$ and $\chi$ are Riccati-Bessel functions, based on the Bessel and Neumann Functions, respectively, in such a way as to be convenient in later calculations. They come from the $r$ equation, which is manipulated so as to give a Bessel equation. To be specific:

$$\psi_l(\rho) = \sqrt{\tfrac{\pi\rho}{2}}\, J_{l+\frac{1}{2}}(\rho), \quad \chi_l(\rho) = -\sqrt{\tfrac{\pi\rho}{2}}\, N_{l+\frac{1}{2}}(\rho) \tag{A.12}$$

It should be noted here that we will also use a linear combination of these functions, which is itself a Riccati-Bessel function as well as a variation on the Hankel function:

$$\zeta_l{}^{(1)}(\rho) = \psi_l(\rho) - i\chi_l(\rho) = \sqrt{\frac{\pi\rho}{2}}\, H_{l+\frac{1}{2}}(\rho) \tag{A.13}$$

Combining the solutions to these equations as prescribed by Eq. (A.9) yields the following series solution:

$$r\Pi = \sum_{l=0}^{\infty}\sum_{m=-l}^{l}\left[(c_l\psi_l(kr) + d_l\chi_l(kr))\right]\left[P_l^{(m)}(\cos\theta)\right]\left[a_m\cos(m\varphi) + b_m\sin(m\varphi)\right] \tag{A.14}$$

with $c_l, d_l, a_m$, and $b_m$ being arbitrary constants and $m$ and $l$ being integers.

## A.4 Boundary Conditions

The basic idea of the boundary conditions for this problem are that we have fields outside the sphere and inside the sphere, and that these fields must be continuous at the surface of the sphere. We have an incoming wave $\overrightarrow{E}^{(i)}$, $\overrightarrow{B}^{(i)}$ which we normalize to unity, i.e. $\left|\overrightarrow{E}^{(i)}\right| = \left|e^{ik^{(I)}z}\right| = 1$. There is a field within the sphere which we shall denote $\overrightarrow{E}^{(w)}$, $\overrightarrow{B}^{(w)}$ and a scattered field which we shall denote $\overrightarrow{E}^{(s)}$, $\overrightarrow{B}^{(s)}$. Considering these fields, we may say

$$\begin{cases} \overrightarrow{E} = \overrightarrow{E}^{(i)} + \overrightarrow{E}^{(s)} & \text{outside the sphere} \\ \overrightarrow{E} = \overrightarrow{E}^{(w)} & \text{inside the sphere} \end{cases} \tag{A.15}$$

For our boundary conditions, we require that the tangential components of the field to be continuous at the surface of the sphere. In spherical coordinates, this means that when $r = a$:

$$\begin{cases} {E_\theta}^{(I)} = {E_\theta}^{(II)} \ , & {E_\varphi}^{(I)} = {E_\varphi}^{(II)} \\ {B_\theta}^{(I)} = {B_\theta}^{(II)} \ , & {B_\varphi}^{(I)} = {B_\varphi}^{(II)} \end{cases} \tag{A.16}$$

When we look at Eq. (A.7), we can see that our boundary conditions may be sufficiently expressed by saying that four quantities remain continuous over the surface. Fully expressed, these are:

$$\begin{cases} \frac{\partial}{\partial r}\left[r\left({}^{e}\Pi^{(i)} + {}^{e}\Pi^{(s)}\right)\right]\big|_{r=a} = \frac{\partial}{\partial r}\left[r^{e}\Pi^{(w)}\right]\big|_{r=a} & (a) \\ \frac{\partial}{\partial r}\left[r\left({}^{m}\Pi^{(i)} + {}^{m}\Pi^{(s)}\right)\right]\big|_{r=a} = \frac{\partial}{\partial r}\left[r^{m}\Pi^{(w)}\right]\big|_{r=a} & (b) \\ k_1^{(I)}\left[r\left({}^{e}\Pi^{(i)} + {}^{e}\Pi^{(s)}\right)\right]\Big|_{r=a} = k_1^{(II)}\left[r^{e}\Pi^{(w)}\right]\Big|_{r=a} & (c) \\ k_2^{(I)}\left[r\left({}^{m}\Pi^{(i)} + {}^{m}\Pi^{(s)}\right)\right]\Big|_{r=a} = k_2^{(II)}\left[r^{m}\Pi^{(w)}\right]\Big|_{r=a} & (d) \end{cases} \tag{A.17}$$

## A.5 Analysis of Potentials

In observing our series solution, Eq. (A.14), we can come to an expansion for the the wave within the sphere as well as the incident and scattered waves. Basically, we determine the unknown coefficients based on the boundary conditions.

The first step is to find the expansion for the incident wave, as we need this information to solve for the other fields. We put our field in spherical coordinates, then use identites involving the exponential function, the most important of which is Bauer's formula:

$$\exp\left[ik^{(I)}r\cos\theta\right] = \sum_{l=0}^{\infty} i^l\left(2l+1\right)\frac{1}{k^{(I)}r}\psi_l\left(k^{(I)}r\right)P_l\left(\cos\theta\right) \tag{A.18}$$

Doing this leads to the following solution for the incoming potential:

$$\begin{cases} r^{e}\Pi^{(i)} = \frac{1}{{k^{(I)}}^2}\sum_{l=1}^{\infty} i^{l-1}\frac{(2l+1)}{l(l+1)}\psi_l\left(k^{(I)}r\right)P_l^{(1)}\left(\cos\theta\right)\cos\varphi & (a) \\ r^{m}\Pi^{(i)} = \frac{1}{{k^{(I)}}^2}\sum_{l=1}^{\infty} i^{l}\frac{k^{(I)}}{k_2{}^{(I)}}\ \frac{(2l+1)}{l(l+1)}\psi_l\left(k^{(I)}r\right)P_l^{(1)}\left(\cos\theta\right)\sin\varphi & (b) \end{cases} \tag{A.19}$$

We use a similar method for the wave within. Since this is our concern in the present problem, I will go over it in more detail. We once again want a solution in the form of our series solution, Eq. (A.14). Note that because the Neumann functions have singularities at the origin, we only include the $\psi$ functions. From our analysis of the incoming wave, we know that our equations can only be satisfied for the unknown potentials for which $m = 1$ and if $a_1 = 0$ for the magnetic potential and $b_1 = 0$ for the electric potential. This gives:

$$\begin{cases} r^e\Pi^{(w)} = \frac{1}{k^{(II)^2}} \sum_{l=1}^{\infty} {}^eA_l\psi_l\left(k^{(II)}r\right) P_l^{(1)}\left(\cos\theta\right)\cos\varphi & (a) \\ r^m\Pi^{(w)} = \frac{i}{k^{(II)}k_2^{(II)}} \sum_{l=1}^{\infty} {}^mA_l\psi_l\left(k^{(II)}r\right) P_l^{(1)}\left(\cos\theta\right)\sin\varphi & (b) \end{cases} \tag{A.20}$$

For the scattered wave, we obtain:

$$\begin{cases} r^e\Pi^{(s)} = \frac{1}{k^{(I)^2}} \sum_{l=1}^{\infty} {}^eB_l\zeta_l^{(1)}\left(k^{(I)}r\right) P_l^{(1)}\left(\cos\theta\right)\cos\varphi & (a) \\ r^m\Pi^{(s)} = \frac{i}{k^{(I)}k_2^{(I)}} \sum_{l=1}^{\infty} {}^mB_l\zeta_l^{(1)}\left(k^{(I)}r\right) P_l^{(1)}\left(\cos\theta\right)\sin\varphi & (b) \end{cases} \tag{A.21}$$

## A.6 Solving for Internal Fields

The final boundary conditions, Eq. (A.17), and our series expansions for the incident, scattered, and interior potentials, Eqs. (A.19)–(A.21), lead us to the following linear relations between the unknown coefficients:

$$\begin{cases} {}^eB_l\frac{1}{k^{(I)}}\zeta_l^{(1)'}\left(k^{(I)}a\right) + \frac{1}{k^{(I)}}i^{l-1}\frac{(2l+1)}{l(l+1)}\psi_l'\left(k^{(I)}a\right) = \frac{1}{k^{(II)}}{}^eA_l\psi_l'\left(k^{(II)}a\right) & (a) \\ {}^mB_l\frac{1}{k_2^{(I)}}\zeta_l^{(1)'}\left(k^{(I)}a\right) + \frac{1}{k_2^{(I)}}i^{l-1}\frac{(2l+1)}{l(l+1)}\psi_l'\left(k^{(I)}a\right) = \frac{1}{k_2^{(II)}}{}^mA_l\psi_l'\left(k^{(II)}a\right) & (b) \\ {}^eB_l\frac{1}{k_2^{(I)}}\zeta_l^{(1)}\left(k^{(I)}a\right) + \frac{1}{k_2^{(I)}}i^{l-1}\frac{(2l+1)}{l(l+1)}\psi_l\left(k^{(I)}a\right) = \frac{1}{k_2^{(II)}}{}^eA_l\psi_l\left(k^{(II)}a\right) & (c) \\ {}^mB_l\frac{1}{k^{(I)}}\zeta_l^{(1)}\left(k^{(I)}a\right) + \frac{1}{k^{(I)}}i^{l-1}\frac{(2l+1)}{l(l+1)}\psi_l\left(k^{(I)}a\right) = \frac{1}{k^{(II)}}{}^mA_l\psi_l\left(k^{(II)}a\right) & (d) \end{cases} \tag{A.22}$$

Note that the addition of a prime to the functions $\psi_l$, ${\zeta_l}^{(1)}$, and later ${P_l}^{(1)}$ denotes differentiation with respect to their arguments.

We are interested with the internal field, characterized by ${}^{e}A_l$ and ${}^{m}A_l$. These coefficients may be solved for by eliminating ${}^{e}B_l$ and ${}^{m}B_l$. (This is where our solution diverges from Born and Wolf, who solve for the $B$ coefficients that characterize the scattered field). Doing this, we obtain:

$$\begin{cases} {}^{e}A_l = i^{l-1}\frac{2l+1}{l(l+1)}\frac{\psi_l{}'\left(k^{(I)}a\right)\zeta_l^{(1)}\left(k^{(I)}a\right)-\psi_l\left(k^{(I)}a\right)\zeta_l^{(1)}{}'\left(k^{(I)}a\right)}{\frac{k^{(I)}}{k^{(II)}}\psi_l{}'\left(k^{(II)}a\right)\zeta_l^{(1)}\left(k^{(I)}a\right)-\frac{k_2^{(I)}}{k_2^{(II)}}\psi_l\left(k^{(II)}a\right)\zeta_l^{(1)}{}'\left(k^{(I)}a\right)} & (a) \\ {}^{m}A_l = i^{l-1}\frac{2l+1}{l(l+1)}\frac{\psi_l{}'\left(k^{(I)}a\right)\zeta_l^{(1)}\left(k^{(I)}a\right)-\psi_l\left(k^{(I)}a\right)\zeta_l^{(1)}{}'\left(k^{(I)}a\right)}{\frac{k_2^{(I)}}{k_2^{(II)}}\psi_l{}'\left(k^{(II)}a\right)\zeta_l^{(1)}\left(k^{(I)}a\right)-\frac{k^{(I)}}{k^{(II)}}\psi_l\left(k^{(II)}a\right)\zeta_l^{(1)}{}'\left(k^{(I)}a\right)} & (b) \end{cases} \tag{A.23}$$

We may now obtain the fields by substituting our solutions for the potentials, Eqs. (A.19)–(A.21), into Eq. (A.7), which ends up giving us:

$$\begin{cases} E_r^{(w)} = \frac{1}{k^{(II)2}}\frac{\cos\varphi}{r^2}\sum_{l=1}^{\infty} l\left(l+1\right){}^{e}A_l\psi_l\left(k^{(II)}r\right)P_l^{(1)}\left(\cos\theta\right) & (a) \\ E_\theta^{(w)} = -\frac{1}{k^{(II)}}\frac{\cos\varphi}{r}\sum_{l=1}^{\infty}\Big[{}^{e}A_l\psi_l{}'\left(k^{(II)}r\right)P_l^{(1)}{}'\left(\cos\theta\right)\sin\theta \\ \qquad\qquad -i\,{}^{m}A_l\psi_l^{(1)}\left(k^{(I)}r\right)P_l^{(1)}\left(\cos\theta\right)\frac{1}{\sin\theta}\Big] & (b) \\ E_\varphi^{(w)} = -\frac{1}{k^{(II)}}\frac{\sin\varphi}{r}\sum_{l=1}^{\infty}\Big[{}^{e}A_l\psi_l{}'\left(k^{(II)}r\right)P_l^{(1)}\left(\cos\theta\right)\frac{1}{\sin\theta} \\ \qquad\qquad -i\,{}^{m}A_l\psi_l\left(k^{(II)}r\right)P_l^{(1)}{}'\left(\cos\theta\right)\sin\theta\Big] & (c) \\ B_r^{(w)} = \frac{1}{k^{(II)}k_2^{(II)}}\frac{\sin\varphi}{r^2}\sum_{l=1}^{\infty} l\left(l+1\right){}^{e}A_l\psi_l\left(k^{(II)}r\right)P_l^{(1)}\left(\cos\theta\right) & (d) \\ B_\theta^{(w)} = -\frac{1}{k_2^{(II)}}\frac{\sin\varphi}{r}\sum_{l=1}^{\infty}\Big[{}^{e}A_l\psi_l\left(k^{(II)}r\right)P_l^{(1)}\left(\cos\theta\right)\frac{1}{\sin\theta} \\ \qquad\qquad -i\,{}^{m}A_l\psi_l{}'\left(k^{(II)}r\right)P_l^{(1)}{}'\left(\cos\theta\right)\sin\theta\Big] & (e) \\ B_\varphi^{(w)} = -\frac{1}{k_2^{(II)}}\frac{\cos\varphi}{r}\sum_{l=1}^{\infty}\Big[{}^{e}A_l\psi_l\left(k^{(II)}r\right)P_l^{(1)}{}'\left(\cos\theta\right)\sin\theta \\ \qquad\qquad -i\,{}^{m}A_l\psi_l{}'\left(k^{(II)}r\right)P_l^{(1)}\left(\cos\theta\right)\frac{1}{\sin\theta}\Big] & (f) \end{cases} \tag{A.24}$$

## A.7 External Fields

Since I used them for my plots of the fields, I thought it appropriate to put in the equations for the incident and scattered fields, as well as the characterizing $B$

coefficients for the scattered fields. These are as follows:

$$\begin{cases} E_r^{(i)} = \exp\left[ik^{(I)}r\cos\theta\right]\,\sin\theta\cos\varphi \\ E_\theta^{(i)} = \exp\left[ik^{(I)}r\cos\theta\right]\,\cos\theta\cos\varphi \\ E_\varphi^{(i)} = -\exp\left[ik^{(I)}r\cos\theta\right]\,\sin\varphi \\ B_r^{(i)} = \frac{ik^{(I)}}{k_2{}^{(I)}}\exp\left[ik^{(I)}r\cos\theta\right]\,\sin\theta\sin\varphi \\ B_\theta^{(i)} = \frac{ik^{(I)}}{k_2{}^{(I)}}\exp\left[ik^{(I)}r\cos\theta\right]\,\cos\theta\sin\varphi \\ B_\varphi^{(i)} = \frac{ik^{(I)}}{k_2{}^{(I)}}\exp\left[ik^{(I)}r\cos\theta\right]\,\cos\varphi \end{cases} \tag{A.25}$$

$$\begin{cases} E_r^{(s)} = \frac{1}{k^{(I)2}}\,\frac{\cos\varphi}{r^2}\sum_{l=1}^{\infty} l\,(l+1)\,{}^eB_l\zeta_l\left(k^{(I)}r\right)P_l^{(1)}\left(\cos\theta\right) & (a) \\ E_\theta^{(s)} = -\frac{1}{k^{(I)}}\,\frac{\cos\varphi}{r}\sum_{l=1}^{\infty}\Big[{}^eB_l\zeta_l{}'\left(k^{(I)}r\right)P_l^{(1)'}\left(\cos\theta\right)\sin\theta \\ \qquad\qquad -i\;{}^mB_l\zeta_l^{(1)}\left(k^{(I)}r\right)P_l^{(1)}\left(\cos\theta\right)\frac{1}{\sin\theta}\Big] & (b) \\ E_\varphi^{(s)} = -\frac{1}{k^{(I)}}\,\frac{\sin\varphi}{r}\sum_{l=1}^{\infty}\Big[{}^eB_l\zeta_l{}'\left(k^{(I)}r\right)P_l^{(1)}\left(\cos\theta\right)\frac{1}{\sin\theta} \\ \qquad\qquad -i\;{}^mB_l\zeta_l\left(k^{(I)}r\right)P_l^{(1)'}\left(\cos\theta\right)\sin\theta\Big] & (c) \\ B_r^{(s)} = \frac{1}{k^{(I)}k_2^{(I)}}\,\frac{\sin\varphi}{r^2}\sum_{l=1}^{\infty} l\,(l+1)\,{}^eB_l\zeta_l\left(k^{(I)}r\right)P_l^{(1)}\left(\cos\theta\right) & (d) \\ B_\theta^{(s)} = -\frac{1}{k_2^{(I)}}\,\frac{\sin\varphi}{r}\sum_{l=1}^{\infty}\Big[{}^eB_l\zeta_l\left(k^{(I)}r\right)P_l^{(1)}\left(\cos\theta\right)\frac{1}{\sin\theta} \\ \qquad\qquad -i\;{}^mB_l\psi_l{}'\left(k^{(II)}r\right)P_l^{(1)'}\left(\cos\theta\right)\sin\theta\Big] & (e) \\ B_\varphi^{(s)} = -\frac{1}{k_2^{(I)}}\,\frac{\cos\varphi}{r}\sum_{l=1}^{\infty}\Big[{}^eB_l\zeta_l\left(k^{(I)}r\right)P_l^{(1)'}\left(\cos\theta\right)\sin\theta \\ \qquad\qquad -i\;{}^mB_l\zeta_l{}'\left(k^{(I)}r\right)P_l^{(1)}\left(\cos\theta\right)\frac{1}{\sin\theta}\Big] & (f) \end{cases} \tag{A.26}$$

where

$$\begin{cases} {}^eB_l = i^{l+1}\frac{2l+1}{l(l+1)}\,\frac{k_2^{(I)}k^{(II)}\psi_l{}'\left(k^{(I)}a\right)\psi_l\left(k^{(II)}a\right)-k_2^{(II)}k^{(I)}\psi_l{}'\left(k^{(II)}a\right)\psi_l\left(k^{(I)}a\right)}{k_2^{(I)}k^{(II)}\zeta_l^{(1)'}\left(k^{(I)}a\right)\psi_l\left(k^{(II)}a\right)-k_2^{(II)}k^{(I)}\psi_l{}'\left(k^{(II)}a\right)\zeta_l^{(1)}\left(k^{(I)}a\right)} & (a) \\ {}^mB_l = i^{l+1}\frac{2l+1}{l(l+1)}\,\frac{k_2^{(I)}k^{(II)}\psi_l\left(k^{(I)}a\right)\psi_l{}'\left(k^{(II)}a\right)-\,k_2^{(II)}k^{(I)}\psi_l{}'\left(k^{(I)}a\right)\psi_l\left(k^{(II)}a\right)}{k_2^{(I)}k^{(II)}\zeta_l^{(1)}\left(k^{(I)}a\right)\psi_l{}'\left(k^{(II)}a\right)-k_2^{(II)}k^{(I)}\zeta_l^{(1)'}\left(k^{(I)}a\right)\psi_l\left(k^{(II)}a\right)} & (b) \end{cases} \tag{A.27}$$

# Appendix B

# Procedure for Coding in MATLAB

The computation of the Mie fields are done using MATLAB. The main program (`mie.m`) calls a subfunction `EAbsorbed` for each point in the plot. The `EAbsorbed` function takes as parameters the $x, y$, and $z$ values of the point as well as the number of terms to be taken in the sum, i.e. it's called with `EAbsorbed(x,y,z,numTerms)`. `EAbsorbed` returns the (complex) components of the electric field vector at the specified point as determined by Eq. (2.1). Once the main program has received the components of the complex field, it computes the magnitude of $\overrightarrow{E}^* \cdot \overrightarrow{E}$ This quantity is proportional to the time-averaged intensity which, for simplicity, will hereafter be referred to as intensity. Since the absorbed energy is directly related to this intensity, we may characterize the energy absorption distribution by characterizing this intensity distribution.

The equations for Mie scattering depend on the absorbtion coefficients ${}^{e}A_l$ and ${}^{m}A_l$, and also depend, as do the absorption coefficients, on the Ricatti-Bessel functions. They also depend on the associated Legendre polynomials of order 1. Thus, subfunctions were created for each of these, with the absorption coefficients as a function of $l$, and the Ricatti-Bessel functions and associated Legendre polynomi-

als as functions of $l$ and their argument, i.e. they are called with `eA(l)`, `mA(l)`, `legP1(l,rho)`, `dlegP1(l,rho)`, `ppsi(l,rho)`, `dpsi(l,rho)`, `zzeta(l,rho)`, `dzeta(l,rho)`. I used "`ppsi`" and "`zzeta`" to avoid confusion with already-existing MATLAB functions. The subfunctions for the associated Legendre polynomials and the Ricatti-Bessel functions, as well as their derivatives, are calculated in accordance with the relations in Section 2.2.

# Index